Materials & Design 126 (2017) 331–338

Contents lists available at ScienceDirect

Materials & Design

journal homepage: www.elsevier.com/locate/matdes

Multifunctional properties and applications of yttrium ferrite nanoparticles prepared by citrate precursor route

Tokeer Ahmad[a,*], Irfan H. Lone[a], S.G. Ansari[b], Jahangeer Ahmed[c], Tansir Ahamad[c], Saad M. Alshehri[c]

[a] Nanochemistry Laboratory, Department of Chemistry, Jamia Millia Islamia, New Delhi 110025, India
[b] Center for Interdisciplinary Research in Basic Sciences, Jamia Millia Islamia, New Delhi 110025, India
[c] Department of Chemistry, College of Science, King Saud University, Riyadh 11451, Saudi Arabia

ARTICLE INFO

Keywords:
Nanoparticles
Multiferroics
Surface area
Wasp-waisted hysteresis
Photocatalysis
DSSC application

ABSTRACT

Yttrium Ferrite nanoparticles were prepared by citrate precursor method at reasonably low temperature. Morphological and elemental studies reveal the formation of monophasic orthorhombic $YFeO_3$ nanoparticles with fairly uniform distribution of nearly spherical particles, high specific surface area of ~338 m^2/g and visible band gap of 2.5 eV. The electrical properties (i.e. dielectric and conductivity) were estimated from ac spectroscopic data as a function of temperature. The wasp-waisted shaped hysteresis loop displayed low H_c of 280 Oe, M_s of 2.0 $emug^{-1}$ and M_r of 0.45 $emug^{-1}$ indicating canted antiferromagnetism with weak ferromagnetic behaviour. In addition to ferromagnetism, a room temperature ferroelectric loop confirmed the multiferroic behaviour of the materials. The humidity sensing properties were investigated from 8 to 80% of RH (Relative Humidity) that showed a linear response with a sensitivity of 16 nF/RH% at room temperature. Dye sensitized solar cell (DSSC) was constructed in combination with TiO_2 powder to determine the photo-conversion efficiency, current density and open circuit voltage. Photocatalytic generation of hydrogen by using $YFeO_3$ nanoparticles has also been studied under the visible light irradiations which showed a significant H_2 evolution reaction rate up to 131.6 μmol h^{-1} g^{-1}.

1. Introduction

In recent years, unique materials with multiple functionalities specific to electronics, sensing and actuator applications are of great scientific and technological interest, classified as ferroelectrics, ferroelastics or ferromagnetics or primary ferroics. These materials have been used in the manufacture of new devices and showed tremendous applications [1]. Efforts have been made for the preparation and study of unexplored properties of novel multiferroic materials like $BiFeO_3$, $BiMnO_3$, $YMnO_3$, $YCrO_3$ and $YFeO_3$ [2–7]. Among them, metal oxides containing iron deliver unique magnetic characteristics at nanoscale. Iron based metal oxides are now being used in microwave industries, magnetic storage devices and digital disk recording media to enhance the performances [8–12]. Synthesis of multiferroic oxides nanostructures with controlled size, shape and crystal structure is also an important concern to researchers [5,6]. Reverse micelles [13,14], sonochemical [15], solvothermal [16], polymeric citrate precursor methods [17], sol-gel [18,19] etc. have been used previously in the synthesis of nanostructured materials. Metal organic precursor method is versatile that can be used in the synthesis of homogeneous nanostructured material with precise control over processing time. Earlier, $YFeO_3$ and iron garnet were reported by various techniques including sol-gel [20], co-precipitation [21,22], sonochemical [23], solid state reaction [24] etc. However, synthesis of pure phase of $YFeO_3$ is rarely reported because of the coexistence of secondary phases like $Y_3Fe_5O_{12}$ during the growth of crystals. For example, presence of metastable nature of the material makes synthesis difficult using the phase-selective synthesis method.

So far, the research has been done on the ferromagnetic properties as a function of particle size and shape. For example, room temperature ferroelectricity was observed in nanocrystalline $YMnO_3$ prepared by polymeric citrate precursor route [5]. Ramaprasad Maiti et al. have synthesized single phase nanocrystalline $YFeO_3$ using solution route [25]. The ferromagnetic hysteresis loops of $YFeO_3$ were obtained up to 300 K and the exchange bias field was observed at 10 K in a field-cooled sample [25]. Popkov et al. have reported the formation of nanocrystalline yttrium ortho-ferrite via thermal treatment of amorphous nanopowders through combustion of glycine-nitrate [26]. $YFeO_3$ film with

* Corresponding author.
E-mail address: tahmad3@jmi.ac.in (T. Ahmad).

http://dx.doi.org/10.1016/j.matdes.2017.04.034
Received 13 January 2017; Received in revised form 8 April 2017; Accepted 11 April 2017
Available online 14 April 2017

hexagonal structure on Si (111) substrate was reported to study the leakage current, ferroelectric and piezoelectric properties [27]. These reports were focused only on the magnetic properties of the synthesized material whereas the material possesses multifunctional properties related to electronics and sensor application [5,22–29]. Recently, $YCrO_3$ nanoparticles were reported for their multiferroic properties using citrate precursor route where un-sintered pellet was used for ferroic measurements due to its high temperature stability and low leakage current [6]. Hence, a detailed study is required to investigate the all feasible properties of the multifunctional material in order to develop the favourable devices. Therefore, in the present study, we report the preparation of $YFeO_3$ nanoparticles by simple and economical Pechini based synthesis route. Structural, morphological, magnetic, photoelectrical, photocatalytic and sensing properties of $YFeO_3$ nanoparticles were studied to explore their multifunctional properties/applications and correlation.

2. Experimental

The following chemical reagents of analytical grade were used in the synthesis of $YFeO_3$ nanoparticles: $Y(NO_3)_3{\cdot}6H_2O$ (99.9%, Alfa Aesar), $Fe(NO_3)_3{\cdot}9H_2O$ (98%, Rankem), ethylene glycol (EG, 99%, SD Fine Chemicals) and citric acid (CA, 99%, Spectrochem). In a typical reaction procedure, 1.4 mL of EG was added into 25 mL of 0.1 M Fe $(NO_3)_3{\cdot}9H_2O$ with constant magnetic stirring followed by the addition of 21.01 g of dried CA. The molar ratio of EG: Citric acid: ferric nitrate was kept as 10:40:1. For the complete dissolution, the reaction mixture was stirred for about 3.5 h at room temperature. Thereafter, 25 mL of 0.1 M of yttrium nitrate was added to the resulting solution and stirred again for 3.5 h. To accelerate the polyesterification between CA and EG, the reaction mixture was heated at 70 °C for 2 h. On heating, the solution changed to viscous gel by removing the excess water and then further heated to135 °C for 20 h. Further, the resulting materials were heated at 300 °C for 3 h under the ambient conditions that resulted into the black coloured precursors. The resulting precursor was ground to fine powder and then calcined at 900 °C for 12 h in air to obtain brownish red coloured $YFeO_3$ powder.

Phase purity and crystallinity of the as-prepared $YFeO_3$ nanoparticles were studied on powder X-ray diffractometer with Ni-filtered Cu-Kα radiations (λ = 1.54056 Å, Bruker's D8 Advance) at a Bragg angle ranging from 10 to 90° with a step size of 0.05°, scan speed of 4°/min and step time interval of 1 s. The crystallite size was calculated using the Scherrer's formula. Fourier transform infrared spectra (FT-IR) of the sample were acquired using Perkin-Elmer's spectrometer (1750). Transmission electron microscopic (TEM) data were collected on FEI TEM operated at 200 kV (Tecnai). Scanning electron microscopic (SEM) and energy dispersive X-ray spectroscopy (EDAX) were carried out on ZEISS EVO 50 SEM operated at 5 kV. Nitrogen adsorption- desorption measurements were conducted at 77 K on Brunauer-Emmett-Teller (BET) surface area analyzer (Nova 2000e, Quantachrome Instruments Limited, USA) from the 'Multipoint BET Method'. The dielectric properties were studied by pelleting the powder to an 8 mm diameter pellet that was prepared at a pressure of 5 Tons. The pellet was prepared by mixing powder with polyvinyl alcohol (PVA, 5% *w/v*) and sintered at 1000 °C for 8 h in air. For contacts, colloidal silver paint (Ted Pella, Inc.) was coated on both faces of pellet that was dried at 100 °C in a convection oven. Dielectric parameters were measured using inductance, capacitance and resistance (LCR) meter (Model 6505 P, Wayne Kerr, UK) with suitable pellet fixture over a frequency range of 100 kHz to 2 MHz while the temperature was varied from 50 to 400 °C. Similarly ferroelectric properties were measured on these pellets by applying different voltage using P-E loop tracer (M/s Radiant Instruments, USA) at 50 kHz. The magnetic properties of the prepared samples were carried out on MPMS SQUID magneto meter at an external magnetic field of ± 60 kOe in the temperature range of 5 to 300 K. The sensing studies for humidity were carried out by varying the different concentrations of moisture level in the dry nitrogen gas as reported elsewhere [28]. Impedance values were recorded at 1 kHz, using Agilent 4294 A impedance analyzer, as a function of moisture level. A special chamber of rectangular shape (10 cm height) in stainless steel was designed and fabricated. A commercial SHAW dew point meter (model no. SADPTR-R, UK) was used for moisture level measurement and control. To ascertain the photo-conversion properties, dye sensitized solar cells (DSSCs) were fabricated, with $YFeO_3$ only, nano-TiO_2 (P25, Degussa, Germany) and 1:1 mixture of the two powders, following the procedures reported elsewhere [29]. Polyethylene glycol (PEG-600) was used for preparing the paste which was blade casted on FTO substrate and used as photo-anode. The cells were characterized under simulated light using solar simulator and various cell parameters were estimated using Kiethley 2400 source meter. The photo-catalytic hydrogen generation of as-prepared nanoparticles was carried out in presence of Na_2S and Na_2SO_3 as the sacrificial agents under visible light irradiation using the procedure as reported elsewhere [30]. For the measurements, 20 mg of the photo-catalyst was dispersed in 75 mL of distilled water containing 0.1 M Na_2S and 0.1 M Na_2SO_3 in a cylindrical glass cell. The solution was purged with nitrogen for 20 min prior to activity tests to remove dissolved oxygen and to maintain inert atmosphere inside the solution. The solution was then exposed to light using 450 W Xe arc lamp (New Port, 6279NS, Ozone-free). The evolution of H_2 gas was estimated using gas chromatography (Perkin Elmer, Clarus 580 GC) equipped with TCD detector.

3. Results and discussions

Fig. 1 shows the X-ray diffraction (XRD) patterns of calcined $YFeO_3$, in which all reflections are indexed to the monophasic orthorhombic distorted perovskite $YFeO_3$ (JCPDS No. 73-1345) with space group (*Pbn*21) and lattice parameters of a = 5.281, b = 5.595 and c = 7.604. The average crystalline size (~72 nm) was estimated by using X-ray line broadening studies of ⟨112⟩ plane. The purity of the $YFeO_3$ compound was further confirmed by FTIR studies before and after calcinations. Fig. 2 indicates the FTIR spectra of $YFeO_3$ nanoparticles before and after the calcination at 900 °C. For un-calcined powder, the stretching of hydroxyl (O—H) group is observed at around 3414 cm^{-1}. The formation of ester linkage before calcination was confirmed by the presence of 1705, 1607 and 1383 cm^{-1} bands which could be due to the C—C, C═O and C—O stretching respectively [31–33]. On calcination, the organic molecules decompose and hence the peak intensities of these organic molecules almost vanished. The M-O finger-print region shows few peaks related to Fe—O bending and stretching vibrations in the form of a broad band before calcination which splits into distinct bands after calcination. Further, the peaks observed at 780 cm^{-1} and

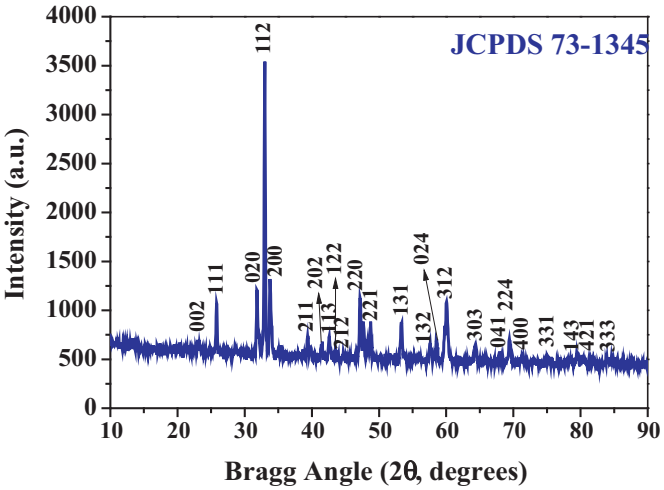

Fig. 1. Power X-ray diffraction pattern of $YFeO_3$ nanoparticles.

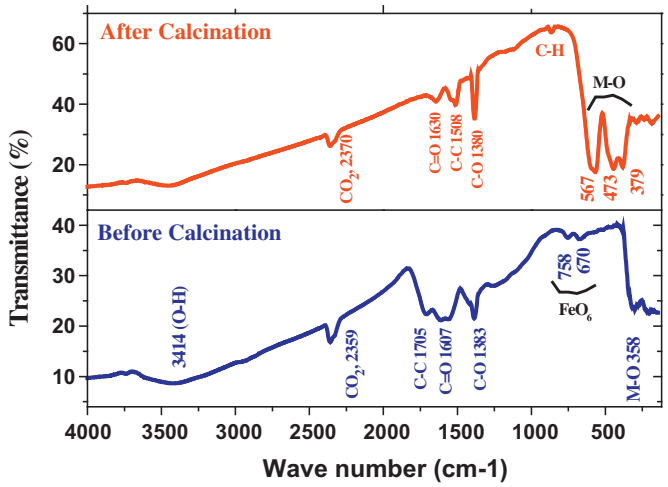

Fig. 2. FTIR spectra of $YFeO_3$ nanoparticles (a) before calcination and (b) after calcination.

567 cm^{-1} are due to the vibration of octahedral FeO_6, which further confirms the formation of $YFeO_3$ pure phase [34]. In both the spectra, a weak band is observed at ~2360 cm^{-1} due to the CO_2 from atmosphere.

Surface texture, average grain size and morphology of the calcined nanomaterials were studied by SEM and TEM examinations as shown in Fig. 3(a, b). The images show crystalline particles with nearly orthorhombic shape along with few hexagonal particles with an average grain size of ~77 nm. For making the TEM images more clear, the high magnification TEM has been given in Fig. 3(c) which additionally helps to find out the average particle size of the prepared nanoparticles. Due the strong magnetic interaction among $YFeO_3$ nanoparticles, some agglomeration could be seen in the SEM images. TEM studies corroborated well with the size estimated using X-ray line broadening studies. The discrete diffraction spots in the diffraction rings of selected area electron diffraction, shown in inset of Fig. 3b, indicate the crystalline nature of $YFeO_3$ nanoparticles. The appearance of concentric rings confirms the polycrystalline nature and could be indexed well with orthorhombic structure of $YFeO_3$ nanoparticles. The composition of as-prepared $YFeO_3$ nanoparticles was further established by energy dispersive analysis of X-rays (EDAX). Fig. 3d shows the atomic % of the elements which express the composition of $YFeO_3$ nanoparticles. EDAX studies of $YFeO_3$ nanoparticles confirm the presence of Y, Fe and O in the prepared sample. The atomic ratio of Y to Fe is approximately 1:1, which showed that the loaded composition has close agreement with the experimentally calculated composition.

The specific surface area of $YFeO_3$ sample was determined by Brunauer-Emmett-Teller (BET) gas adsorption method and the specific surface area of the sample was found to be very high ~338 m^2/g as compared to earlier reported values of 11.7 m^2/g and 9.6 m^2/g [35,36]. The pore size of these nanoparticles was estimated by using Barrett-Joyner-Halenda (BJH) method with a predominance of mesopores of diameter 16.4 Å. Using Kubelka-Munk function F(R), the energy band gap of $YFeO_3$ nanoparticles was estimated from the UV visible diffuse reflectance spectroscopy [37]. By plotting $[F(R)E_g]^n$ versus E, the band gap was obtained by the extrapolation of linear plot to $[F(R)E_g]^n = 0$ as shown in Fig. 4. The direct band gap value of 2.50 eV was estimated from the linear plot putting the value of n = 2 for $YFeO_3$ nanoparticles. This value of band gap lies in the visible light region which showed that the present material can be used for photocatalytic splitting of water in hydrogen generation and DSSC fabrication.

The dielectric properties were studied by the variation of frequency and temperature using LCR meter. The dielectric constant and dielectric loss (ε and D) for the synthesized $YFeO_3$ nanoparticles at room temperature is shown in Fig. 5a. Increase in frequency, decreases both the dielectric constant and dielectric loss values and saturates at 1 MHz. This variation can be explained by the fact that at higher frequency the electric dipoles lag behind the variation of applied field. This type of behaviour was well reported on the basis of Maxwell-Wagner interfacial polarization [37,38]. The variation in dielectric constant (ε) and dielectric loss (D) as a function of temperature at 500 kHz frequency

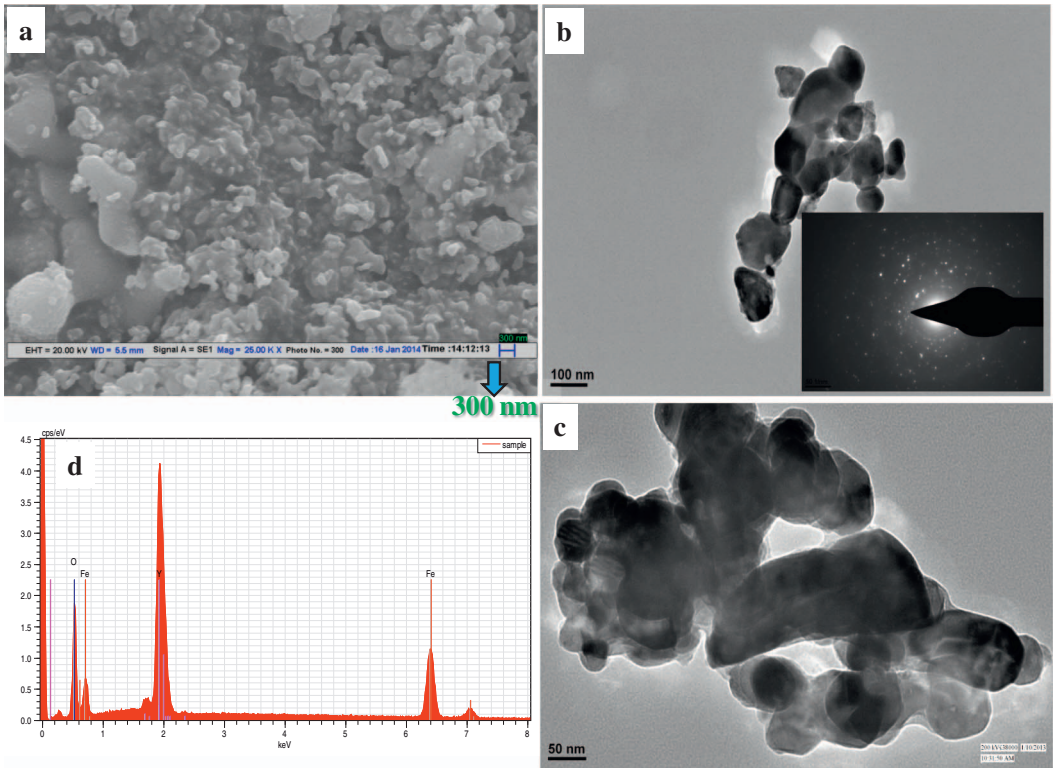

Fig. 3. (a) SEM, (b and c) TEM image, SAED pattern is shown as inset and (d) EDAX spectra of $YFeO_3$ nanoparticles.

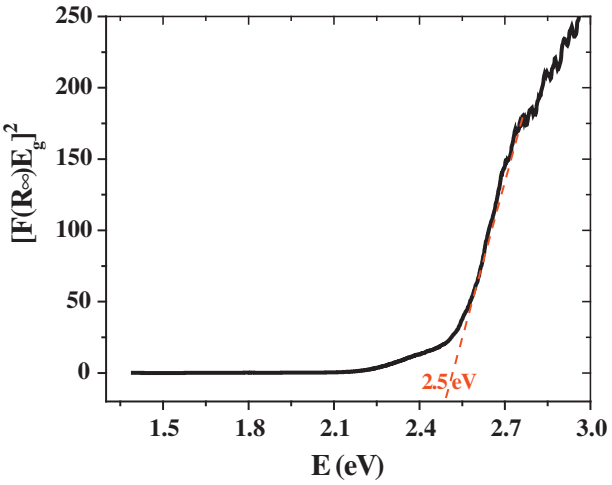

Fig. 4. UV Visible diffuse reflectance band gap plot of $YFeO_3$ nanoparticles.

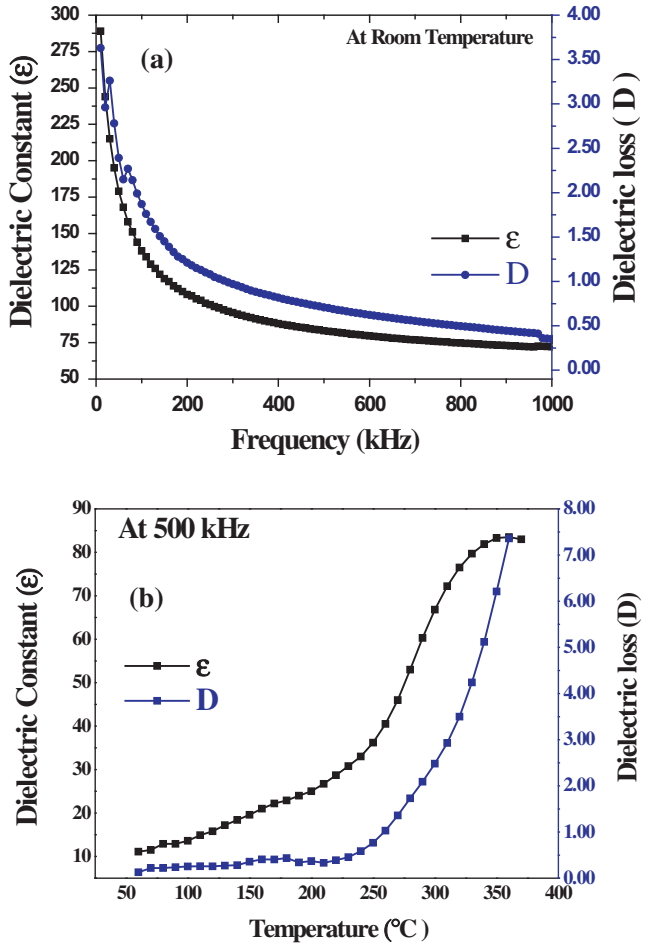

Fig. 5. Variation of dielectric constant and dielectric loss of $YFeO_3$ nanoparticles as a function of (a) frequency at room temperature and (b) temperature at 500 kHz.

is shown in Fig. 5b. Both dielectric parameters increased from ε = 11, D = 0.12 to ε = 83.5, D = 7.6, with increase in temperature from 60 °C to 360 °C respectively. The value of ac conductivity increases following the increase of temperature and frequency. In case of polycrystalline compounds there exists large number of conducting grain and these grains are separated by insulating grain boundaries. In present study, the type of conductivity behaviour are correlated with other ferrite systems which are associated to the conducting grains separated by grain boundaries [39,40]. Below the temperature range (200 °C–250 °C), the change in the dielectric parameters was found to be small, thereafter sharp increase was noted. This could be due to the orientation of dipoles and gains' high mobility due to space charge, results in the large dielectric permittivity [40].

The variation in ac conductivity with temperature was studied by varying frequency from 100 kHz to 2 MHz as shown in Fig. 6a. Initially the ac conductivity slightly increases with increasing temperature till 270 °C, and then sharply increases with the increase of temperature. It has been observed that the value of ac conductivity not only depends on temperature but also varies with frequency. This nature of variation may be interpreted by the existence of highly conducting grains separated by grain boundaries, as were also observed in many other ferrite systems [40]. The dc conductivity (σ_{dc}) is plotted with the function of inverse temperature as shown in Fig. 6b which follows the relation.

$$\sigma = \sigma_0 \exp\left(-\frac{E_{cond}}{k_B T}\right)$$

where E_{cond} is the conduction activation energy and σ_0 is the pre-exponential term. The activation energy (E_{cond}) was found to be 0.4 eV from the plot (Fig. 6b), which suggests that the ionic charge and grain boundary defects are responsible for thermal conductivity. Not only is the conductance but impedance analysis was also found to be useful to determine the electrical properties of $YFeO_3$ nanoparticles. Fig. 6c shows variation in the impedance with frequency and temperature. It is found that the impedance decreases as temperature and frequency increase with saturation above the 275 °C as against the ac conductivity behaviour.

The magnetic properties of synthesized material were studied as a function of temperature from 5 K to 300 K in an external magnetic field of ± 60 kOe. Fig. 7a shows the variation in molar susceptibility with temperature which indicates the presence of weak ferromagnetic interactions. The origin of these types of interactions could be related to the alignments of Fe moments in $YFeO_3$ which are not strictly antiparallel but are slightly canted [41]. To obtain information about the ferromagnetic interaction, M-H studies were carried out at − 268 °C (5 K) and the data is shown as Fig. 7b. The appearance of wasp-wasted shaped hysteresis loop (see inset of Fig. 7b), indicates that there are better values of saturation and remanent magnetization but less value of coercive field. This phenomenon results from the weak ferromagnetic ordering in the sample as observed from molar susceptibility measurement (Fig. 7a). The value of remanent magnetization (M_r) and coercive field (H_c) for $YFeO_3$ nanoparticles are about 280 Oe and 0.45 emu/g respectively, while the saturated magnetization (M_s) is found to be ~2.0 emu/g. The obtained values of these magnetic properties of as-prepared $YFeO_3$ nanoparticles are slightly greater with the reported values [40,42,43]. This happens because the prepared magnetic materials are in the nano-regime and each nanoparticle behaves as single domain which contributes to the enhancement of the magnetic properties. The magnetic properties of $YFeO_3$ nanoparticles indicate the presence of remanent magnetization. This could be due to the distorted perovskite structure of $YFeO_3$ nanoparticles with an orthorhombic unit cell [42,43]. The position of yttrium ions are responsible for the distortion of $YFeO_3$ compound from the ideal perovskite structure in which Fe^{3+} ions form octahedral structure; as a three-dimensional FeO_6 octahedral. In three dimensional network of FeO_6 octahedral, the super-exchange bond (Fe−O−Fe) between the two ions is provided by the common apex of anions (O^{2-}) between two adjacent octahedra. The alignment of Fe moments is not completely antiparallel but slightly canted, this leads to the small net magnetization which attributes to the weak ferromagnetic behaviour [41].

Fig. 8 shows the polarization versus electric field (P-E) graph of nanocrystalline $YFeO_3$ obtained by varying the applied electric field at 50 kHz. A well resolved ferroelectric loop was obtained from the P-E

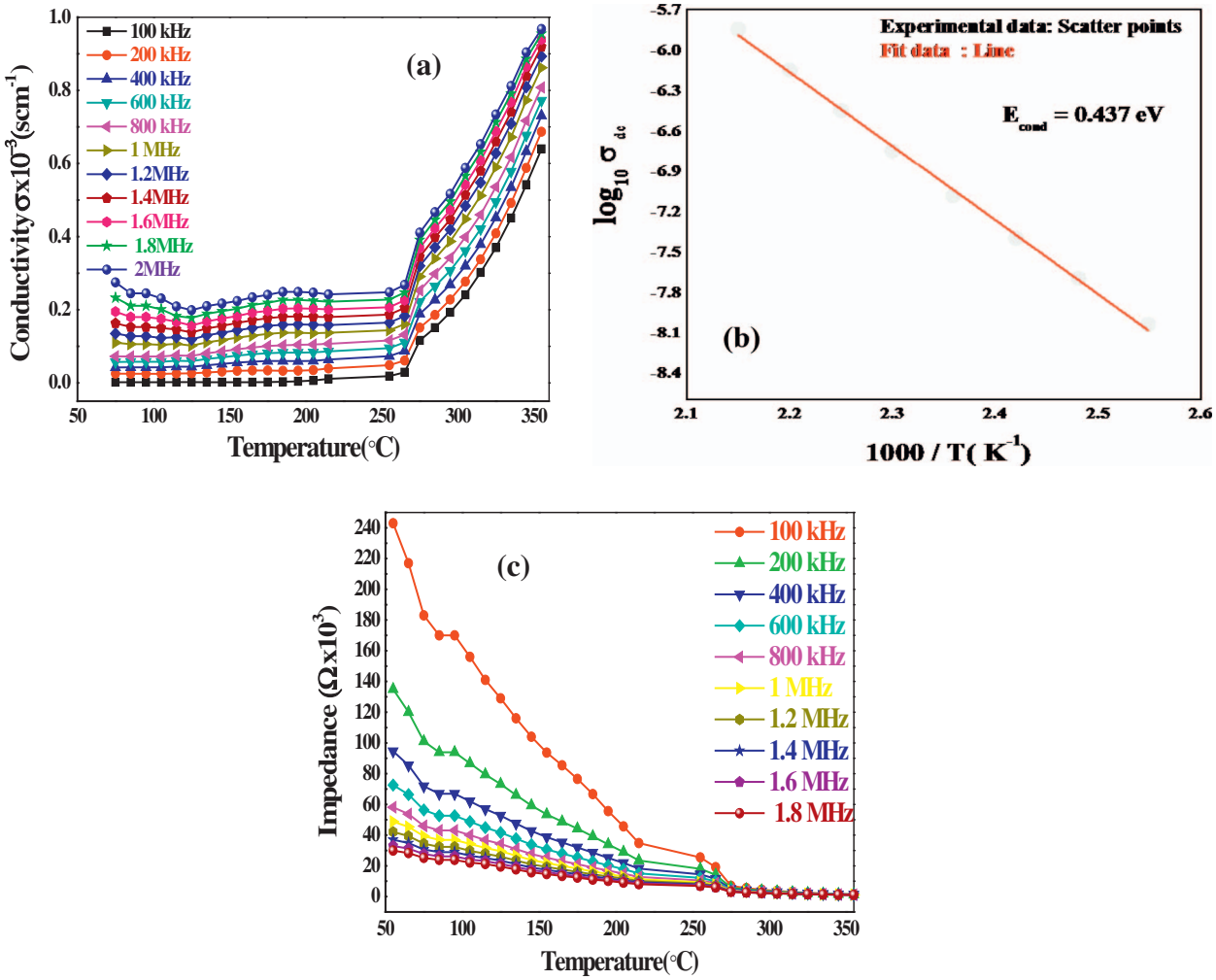

Fig. 6. (a) Temperature variation of ac conductivity, (b) Arrhenius plot and (c) temperature variation of the impedance of the $YFeO_3$ nanoparticles.

hysteresis loop measured at room temperature showing relatively higher remanent polarization P_r (0.0017 μC/cm^2), saturation polarization P_s (0.026 μC/cm^2) and coercive field E_c of (− 3.27 kV/cm). The values obtained at low applied field were found better than the reported values of bulk material with same chemical composition [44]. $YFeO_3$ falls in the centrosymmetric orthoferrite family which is known to be non-ferroelectric in nature, but as-prepared $YFeO_3$ nanoparticles surprisingly show the room temperature ferroelectric behaviour. Similar results were reported for $SmFeO_3$ compound earlier [44]. In these cases, the anomalous behaviour of polarization was due to non-equivalent spin pairs in the antiferromagnetic order and this polarization is known as antiferromagnetic ordering induced ferroelectricity [45].

Moreover, $YFeO_3$ nanoparticles were also used for humidity sensing to explore the sensing properties. Initially pelletized $YFeO_3$ nanoparticles were allowed to pass dry N_2 gas at 2.5 ppm moisture level and were then exposed to different humidity levels (8 to 80%). The capacitance of the pellet was measured at 1 kHz, which is plotted as Fig. 9. It is clear from the curve that capacitance increases with relative humidity (RH%) with slight non-linearity (~19%). The sensitivity was calculated from the linear fit data shown as dotted line which is ~16 nF/RH% and linearity of about 81% [45]. The humidity sensing studies were found impressing with reported data. For example, Kotnala et al. developed humidity sensor using magnesium ferrite ($MgFe_2O_4$), substituted with different ratios of lithium and tested in the RH range of 10%–80% at room temperature [46]. They found that at lower RH, the sensitivity increased due to better electron donation from water vapours to the bulk surface in addition to higher surface area and hence better adsorption/desorption of water vapours. A similar observation is noticed in the present study indicating that the synthesized material is behaving in expected nature and analogous to reported data [46].

Additionally, the developed DSSC studies were also investigated by I-V characteristics using simulated light source. DSSC parameters like open circuit voltage (V_{oc}), short circuit current densities (J_{sc}), and efficiency were measured for cell. The cell parameters for nano-TiO_2, nano-$YFeO_3$ and the mixture of the two powders are listed in Table 1. The graph between the current density (J_{sc}) and voltage is shown in Fig. 10. It is found that pure TiO_2 shows lowest conversion efficiency, while $YFeO_3$ nanoparticles resulted in two orders higher efficiency. While in case of mixed powder ($YFeO_3$ and TiO_2), a slightly better efficiency was observed, as shown in Fig. 10. The initial studies on photo conversion of $YFeO_3$ nanoparticles has been found to show sufficient conversion efficiency as comparable to that of nano-TiO_2, which can be related to photocatalytic properties and higher surface area available for dye adsorption.

The photocatalytic hydrogen generation of as-prepared nanoparticles was carried out in presence of Na_2S and Na_2SO_3 as the sacrificial agents under visible light irradiation as shown in Fig. 11. The visible-light-induced splitting of water by using $YFeO_3$ nanoparticles showed a significant H_2 evolution reaction rate up to 131.6 μmol h^{-1} g^{-1}. The linear relation of hydrogen evolution with time correlates with the good photocatalytic activity of $YFeO_3$ nanoparticles under visible light irradiation.

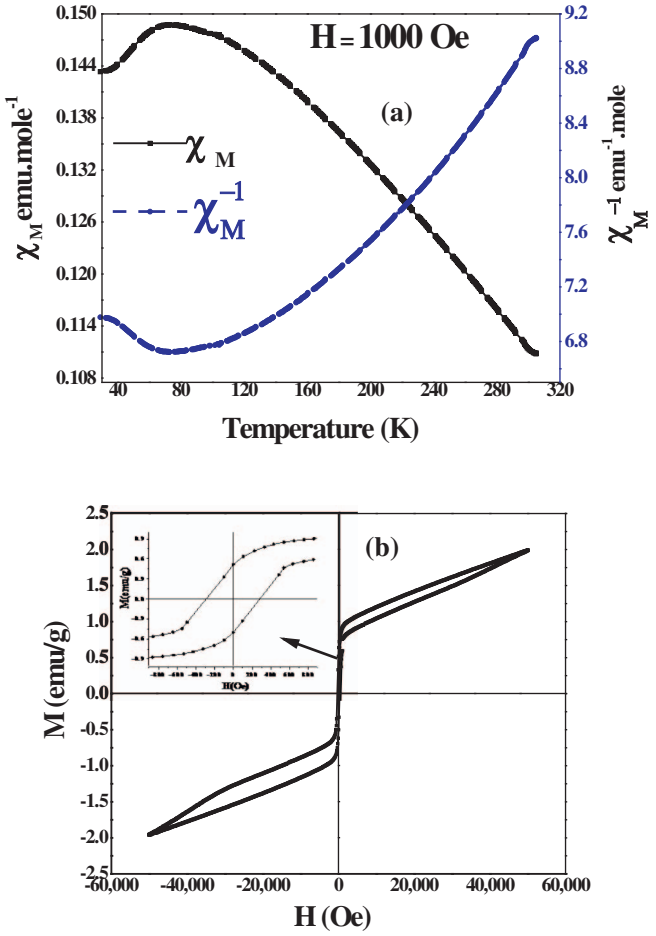

Fig. 7. (a) Temperature dependence of molar susceptibility and (b) M-H curve of $YFeO_3$ nanoparticles at 5 K. Inset shows the closer look of hysteresis.

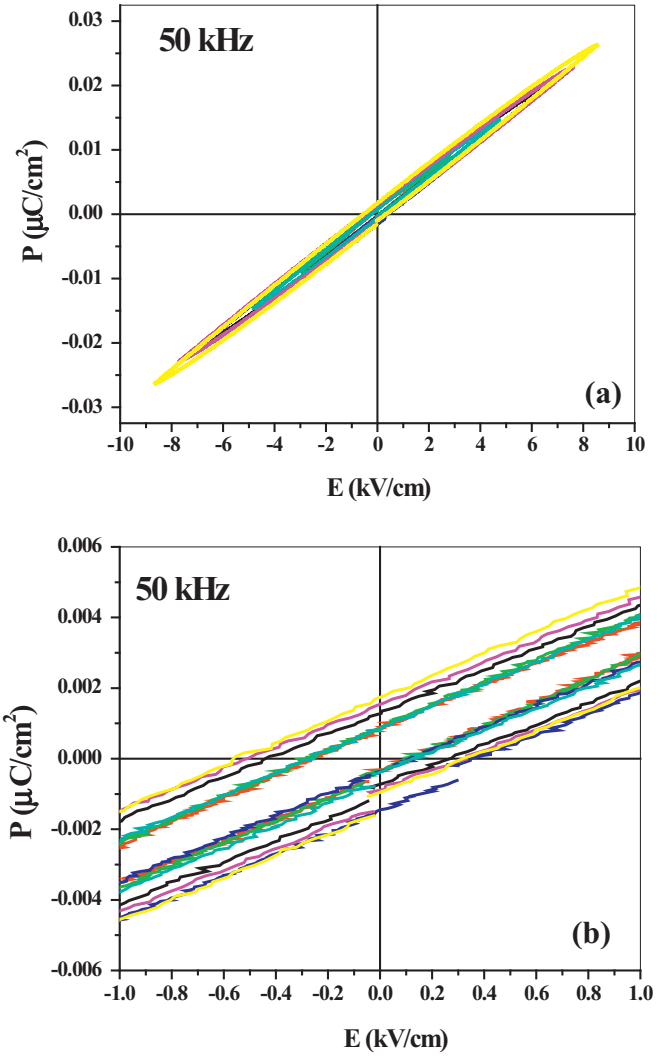

Fig. 8. (a) P-E hysteresis loops and (b) closer image of hysteresis of $YFeO_3$ nanoparticles measured at different electric fields at the frequency of 50 kHz.

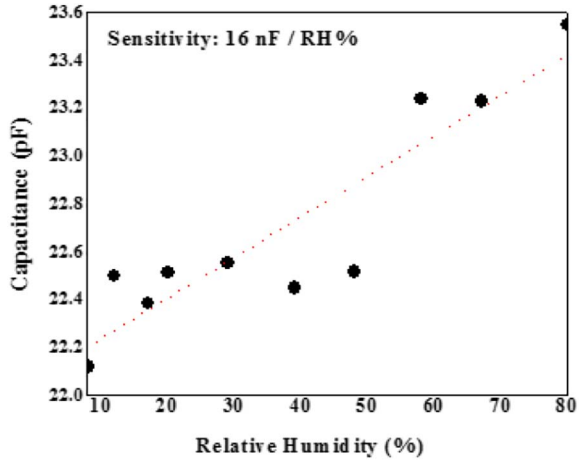

Fig. 9. Variation of capacitance with relative humidity of $YFeO_3$ nanoparticles.

4. Conclusions

We have successfully synthesized multiferroic $YFeO_3$ by firing gel precursor process. XRD and FTIR studies indicated pure phase and crystalline nature of $YFeO_3$ with orthorhombic structure at 900 °C. The TEM grain size (77 nm) is well corroborated with the X-ray size (72 nm) studies. High surface area of 338 m^2/g was estimated by using multi-point BET method. Reflectance measurement showed optical energy band gap of 2.5 eV of as-prepared nanoparticles that lies in visible range. Multifunctional properties of the $YFeO_3$ nanomaterials were established in terms of electric, magnetic, sensing and photo conversion characteristics. The appearance of hysteresis in both electric and magnetic studies confirms the multiferroic nature of $YFeO_3$ nanoparticles. The fabricated dye sensitized solar cell showed better power conversion efficiency as compared to conventional TiO_2 system and was further increased for $YFeO_3$-TiO_2 system. As-prepared nanoparticles also show photocatalytic hydrogen generation characteristics.

Competing financial interests

The authors declare no competing financial interests.

Acknowledgements

The authors thank the Innovative Research Activities of Jamia Millia Islamia, New Delhi (AC-6(15)/RO/2014) for the support. The authors also extend their appreciation to the Deanship of Scientific Research at King Saud University for funding this work through research group (RGP-1438-026). Authors thank the AIIMS New Delhi for electron microscopic studies, ICMS JNCASR Bangalore for photocatalytic splitting of water and Professor K. V. Ramanujachary (Rowan University, USA) for conducting and analyzing the magnetic measurements. Dr. V. R. Reddy (UGC-DAE Indore) was highly acknowledged for P-E measurements. IHL thanks to UGC New Delhi for the grant of

Table 1
DSSC data of TiO_2, $YFeO_3$ and $YFeO_3$-TiO_2 systems.

Material	I_{sc}	V_{oc}	%age
$YFeO_3$	1.51E − 06	1.5	0.01458
$YFeO_3$-TiO_2	2.10E − 06	1.5	0.01713
TiO_2	6.15E − 04	1.1	0.00078

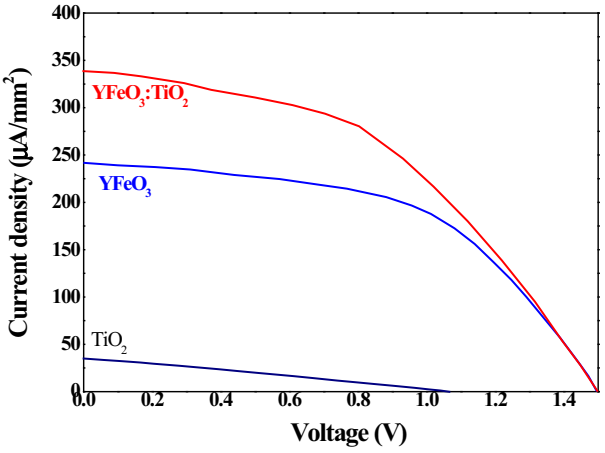

Fig. 10. Current density–voltage measurements of TiO_2, $YFeO_3$ and TiO_2-$YFeO_3$ systems respectively (area of the cell: 2.5 mm × 2.5 mm).

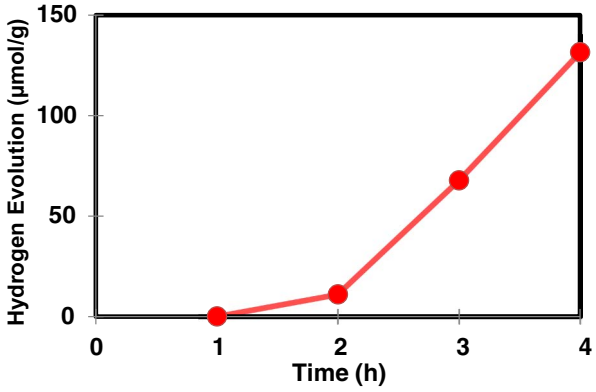

Fig. 11. Hydrogen generation as a function of time with $YFeO_3$ nanoparticles under irradiation of visible light using Na_2S and Na_2SO_3 as the sacrificial agents.

research fellowship.

References

[1] A.N. Hill, Why are there so few magnetic ferroelectrics, J. Phys. Chem. B 104 (2000) 6694–6709.
[2] J. Lv, H. Zhao, M. Wu, X. Lou, J. Wu, Modulating the electric and magnetic properties of $BiFeO_3$ ceramics, Mater. Des. (2017), http://dx.doi.org/10.1016/j.matdes.2017.04.007.
[3] K.Y. Yuan, M. Noda, M. Okuyama, Structural and multiferroic properties of $BiFeO_3$ thin films at room temperature, J. Appl. Phys. 96 (2004) 3399–3403.
[4] A.S. Moreira, S. Parashar, R.A. Raju, S.Y. Zhao, A.K. Cheetham, C.N.R. Rao, Evidence for the likely occurrence of magnetoferroelectricity in the simple perovskite, $BiMnO_3$, Solid State Commun. 122 (2002) 49–52.
[5] T. Ahmad, I.H. Lone, M. Ubaidullah, Structural characterization and multiferroic properties of hexagonal nano-sized $YMnO_3$ developed by low temperature precursor route, RSC Adv. 5 (2015) 58065–58071.
[6] T. Ahmad, I.H. Lone, Citrate precursor synthesis and multifunctional properties of $YCrO_3$ nanoparticles, New J. Chem. 40 (2016) 3216–3224.
[7] L.H. Yin, W.H. Song, L.X. Jiao, B.W. Wu, L. Lj, W. Tang, X.B. Zhu, Z.R. Yang, J.M. Dai, R.L. Zhang, Y.P. Sun, A study of the magnetic and dielectric properties of $YFe_{0.5}Cr_{0.5}O_3$, Solid State Commun. 150 (2010) 1074–1076.
[8] G. Ji, S. Tang, B. Xu, B. Gu, Y. Du, Synthesis of $CoFe_2O_4$ nanowire arrays by sol-gel template method, Chem. Phys. Lett. 379 (2003) 484–489.
[9] A. Khan, P. Chen, P. Boolchand, P.G. Smirniotis, Modified nano-crystalline ferrites for high-temperature WGS membrane reactor applications, J. Catal. 253 (2008) 91–104.
[10] M. Srivastava, A.K. Ojha, S. Chaubey, A. Materny, A polyethylene glycol-assisted route to synthesize $Pb(Ni_{1/3}Nb_{2/3})O_3$-$PbTiO_3$ in pure perovskite phase, J. Alloys Compd. 481 (2009) 510–515.
[11] X. Wang, L.Y. Wang, I.I. Lim, S. Lim, K. Bao, D. Mott, H.Y. Park, J. Luo, L.S. Hao, C.J. Zhong, Synthesis, characterization and potential application of MnZn ferrite and MnZn ferrite@Au nanoparticles, J. Nanosci. Nanotechnol. 9 (2009) 3005–3012.
[12] K.C. Mouli, T. Joseph, K. Ramam, Synthesis and magnetic studies of Co-Ni-Zn ferrite nanocrystals, J. Nanosci. Nanotechnol. 9 (2009) 5596–5599.
[13] T. Ahmad, A.K. Ganguli, Synthesis of nanometer-sized particles of barium orthotitanate prepared through a modified reverse micellar route: structural characterization, phase stability and dielectric properties, J. Mater. Res. 19 (2004) 2905–2912.
[14] A.K. Ganguli, S. Vaidya, T. Ahmad, Synthesis of nanocrystalline materials through reverse micelles: a versatile methodology for synthesis of complex metal oxides, Bull. Mater. Sci. 31 (2008) 415–419.
[15] I.A. Wani, T. Ahmad, Size and shape dependant antifungal activity of gold nanoparticles: a case study of Candida, Colloids Surf. B 101 (2013) 162–170.
[16] T. Ahmad, S. Khatoon, K. Coolahan, S.E. Lofland, Structural characterization, optical and magnetic properties of Ni-doped CdO dilute magnetic semiconductor nanoparticles, J. Mater. Res. 28 (2013) 1245–1253.
[17] O.A. Al-Hartomy, M. Ubaidullah, S. Khatoon, J.H. Madani, T. Ahmad, Synthesis, characterization and dielectric properties of nanocrystalline $Ba_{1-x}Pb_xZrO_3$ ($0 \le x \le 0.75$) by polymeric citrate precursor route, J. Mater. Res. 27 (2012) 2479–2488.
[18] T.F. Zhang, X.G. Tang, Q.X. Liu, Y.P. Jiang, L.L. Jiang, L. Luo, Optical and dielectric properties of $PbZrO_3$ thin films prepared by a sol-gel process for energy-storage application, Mater. Des. 90 (2016) 410–415.
[19] S. Zahi, Nickel-zinc ferrite fabricated by sol-gel route and application in high-temperature superconducting magnetic energy storage for voltage sag solving, Mater. Des. 31 (2010) 1848–1853.
[20] A.V. Racu, D.H. Ursu, O.V. Kuliukova, C. Logofatu, A. Leca, M. Miclau, Direct low temperature hydrothermal synthesis of $YFeO_3$ microcrystals, Mater. Lett. 140 (2015) 107–110.
[21] M.M. Rashad, M.M. Hessien, A. El-Midany, I.A. Ibrahim, Effect of synthesis conditions on the preparation of YIG powders via co-precipitation method, J. Magn. Magn. Mater. 321 (2009) 3752–3757.
[22] N.A. Tien, O.V. Almjasheva, I.Y. Mittova, O.V. Stognei, S.A. Soldatenko, Synthesis and magnetic properties of $YFeO_3$ nanocrystals, Inorg. Mater. 45 (2009) 1304–1308.
[23] J. Pinkas, V. Reichlova, A. Serafimidisova, Z. Moravec, R. Zboril, D. Jancik, P. Bezdicka, Sonochemical synthesis of amorphous yttrium iron oxides embedded in acetate matrix and their controlled thermal crystallization toward garnet ($Y_3Fe_5O_{12}$) and perovskite ($YFeO_3$) nanostructures, J. Phys. Chem. C 114 (2010) 13557–13564.
[24] S.D. Schmool, N. Keller, M. Guyot, R. Krishnan, M.E. Tessier, Evidence of very high coercive fields in orthoferrite phases of PLD grown thin films, J. Magn. Magn. Mater. 195 (1999) 291–298.
[25] R. Maiti, S. Basu, D. Chakravorty, Synthesis of nanocrystalline $YFeO_3$ and its magnetic properties, J. Magn. Magn. Mater. 321 (2009) 3274–3277.
[26] V.I. Popkov, O.V. Almjasheva, V.V. Gusarov, The investigation of the structure control possibility of nanocrystalline yttrium orthoferrite in its synthesis from amorphous powders, Russ. J. Appl. Chem. 87 (2014) 1417–1421.
[27] Z. Run-Lan, C. Chang-Le, Z. Yun-Jie, X. Hui, D. Xiang-Lei, Ke-Xin, Ferroelectricity in hexagonal $YFeO_3$ film at room temperature, Chin. Phys. B 24 (2015) 017701–017705.
[28] L. Kumar, D.D. Saha, S.D.A. Khan, K. Sengupta, T.A. Islam, A medium-range hygrometer using nano-porous thin film of γ-Al_2O_3 with electronics phase detection, IEEE Sensors J. 12 (2012) 1625–1632.
[29] M. Ye, M. Lv, C. Chen, J. Iocozzia, C. Lin, Z. Lin, Low-cost Nanomaterials: Toward Greener and More Efficient Energy Applications, Springer-Verlag, London, 2014 (Ch. 5).
[30] S.R. Lingampalli, U.K. Gautam, C.N.R. Rao, Highly efficient photocatalytic hydrogen generation by solution-processed ZnO/Pt/CdS, ZnO/Pt/$Cd_{1-x}Zn_xS$ and ZnO/Pt/$CdS_{1-x}Se_x$ hybrid nanostructures, Energy Environ. Sci. 6 (2013) 3589–3594.
[31] Y. Zhang, J. Yang, J. Xu, Q. Gao, Z. Hong, Controllable synthesis of hexagonal and orthorhombic $YFeO_3$ and their visible-light photocatalytic activity, Mater. Lett. 81 (2012) 1–4.
[32] K. Nakamato, Infrared and Raman Spectra of Inorganic and Coordination Compounds, fourth ed., 242 Wiley-Interscience, 1986.
[33] L.J. Bellamy, The Infrared Spectra of Complex Molecules, second ed., 425 Methuen & Co., 1958.
[34] R.K. Mishra, D.K. Pradhan, R.N.P. Choudhary, A. Banerjee, Effect of yttrium on improvement of dielectric properties and magnetic switching behavior in $BiFeO_3$, J. Phys. Condens. Matter 20 (2008) 1–6045218.
[35] P. Tang, H. Chen, F. Cao, G. Pan, Magnetically recoverable and visible-light-driven nanocrystalline $YFeO_3$ photocatalysts, Cat. Sci. Technol. 1 (2011) 1145–1148.
[36] P. Tang, H. Sun, H. Chen, F. Cao, Hydrothermal processing-assisted synthesis of nanocrystalline $YFeO_3$ and its visible-light photocatalytic activity, Curr. Nanosci. 8 (2012) 64–67.
[37] G. Kortum, Reflectance Spectroscopy, Springer-Verlag, 1969, pp. 170–216.
[38] K.W. Wagner, Zur theorie der unvoll Kommener dielektrika, Ann. Phys. 40 (1993) 817–855.
[39] C.G. Koops, On the dispersion of resistivity and dielectric constant of some

semiconductors at audio frequencies, Phys. Rev. 83 (1951) 121–124.
[40] S. Zahi, R.A. Dauda, M.A. Hashim, A comparative study of nickel–zinc ferrites by sol-gel route and solid-state reaction, Mater. Chem. Phys. 106 (2007) 452–456.
[41] S. Mathur, M. Veith, R. Rapalaviciute, H. Shen, G. Goya, W. Martins-Filho, T. Berquo, Molecule derived synthesis of nanocrystalline $YFeO_3$ and investigations on its weak ferromagnetic behavior, Chem. Mater. 16 (2004) 1906–1913.
[42] S. Geller, E.A. Wood, Crystallographic studies of perovskite-like compounds. I. Rare earth orthoferrites and $YFeO_3$, $YCrO_3$, $YAlO_3$, Acta Crystallogr. 9 (1956) 563–568.
[43] S. Geller, Crystal structure of gadolinium orthoferrite, $GdFeO_3$, J. Chem. Phys. 24 (1956) 1236–1238.
[44] M. Shang, C. Zhang, T. Zhang, L. Yuan, L. Ge, H. Yuan, S. Feng, The multiferroic perovskite $YFeO_3$, Appl. Phys. Lett. 102 (2013) 1–3062903.
[45] J.H. Lee, Y.K. Jeong, J.H. Park, M. Oak, H.M. Jang, J.Y. Son, J.F. Scott, Spin-canting-induced improper ferroelectricity and spontaneous magnetization reversal in $SmFeO_3$, Phys. Rev. Lett. 107 (2011) 1–5117201.
[46] R.K. Kotnala, J. Shah, B. Singh, H. Kishan, S. Singh, S.K. Dhawan, A. Sengupta, Humidity response of Li-substituted magnesium ferrite, Sensors Actuators B Chem. 129 (2008) 909–914.